35th Annual International Conference of the IEEE EMBS
Osaka, Japan, 3 - 7 July, 2013

Employing *in-vivo* Molecular Imaging in Simulating and Validating Tumor Growth

Eleftheria Tzamali, Rosy Favicchio, Alexandros Roniotis, Georgios Tzedakis, Giorgos Grekas, Jorge Ripoll, Kostas Marias, Giannis Zacharakis, and Vangelis Sakkalis

Abstract—**During the last decades, especially via the EU initiative related to the Virtual Physiological Human, significant progress has been made in advancing "in-silico" computational models to produce accurate and reliable tumor growth simulations. However, currently most attempts to validate the outcome of the models are either done in-vitro or ex-vivo after tumor resection. In this work, we incorporate information provided by fluorescence molecular tomography performed in-vivo into a mathematical model that describes tumor growth. The outcome is validated against tumor evolution snapshots captured in-vivo using advanced molecular probes in laboratory animals. The simulations are inline with the actual in-vivo growth and although alternative modeling parameters can lead to similar results challenging for additional microscopic information and imaging modalities to drive the in-silico models, they all show that hypoxia plays a dominant role in the evolution of the tumor under study.**

I. Introduction

Considerable progress in understanding cancer on the molecular, cellular and tissue level has undoubtedly provided new powerful weapons for fighting the disease. Furthermore, a number of computational (in-silico) models have been developed in order to study the various phases and scales of cancer describing different levels of biocomplexity [1, 2]. Most of the approaches in *in-silico* oncology have been targeted to the provision of insight into the tumor growth mechanisms (cancer biology modeling). Yet, a parallel need of crucial importance is to serve the above models with advanced anatomical and functional imaging methods able to localize and image the tumor, while being appropriate for in vivo staining, such as fluorescence molecular probes, and proteins.

Research supported in part by the TUMOR (FP7-ICT-2009.5.4-247754) project and by the FP7 EU Grant "FMT-XCT".

V. Sakkalis, E. Tzamali, A. Roniotis; G. Tzedakis, G. Grekas, K. Marias are with the Institute of Computer Science, Foundation for Research and Technology – Hellas, N. Plastira 100, 70013, Heraklion Crete, Greece (e-mail:{sakkalis; tzamali; roniotis; gtzedaki; ggrekas; kmarias}@ics.forth.gr).

R. Favicchio was with the Institute for Electronic Structure and Laser, Foundation for Research and Technology – Hellas, N. Plastira 100, Heraklion Crete, Greece. She is now with the Comprehensive Cancer Imaging Center, Imperial College, London UK (e-mail: r.favicchio@imperial.ac.uk).

J. Ripoll was with the Institute for Electronic Structure and Laser, Foundation for Research and Technology – Hellas, N. Plastira 100, Heraklion Crete, Greece. He is now with the Dept. of Bioengineering and Aerospace Engineering, Universidad Carlos III of Madrid, Avda. de la Universidad 30,28911 Leganés, Madrid Spain (e-mail: jorge.ripoll@uc3m.es)

G. Zacharakis is with the Institute for Electronic Structure and Laser, Foundation for Research and Technology – Hellas, N. Plastira 100, 70013, Heraklion Crete, Greece.

On the other hand, advances in biomedical imaging technologies brought about in recent years have revolutionized the way we approach a variety of medical and biological questions. Novel technological approaches have shed light into biological processes and function, with the field of *in vivo* molecular imaging being recognized as one of the most influential for translational research [3, 4]. By connecting gene activity with physiology the molecular basis of health and disease can be studied and understood. Important factors of disease and especially cancer, such as angiogenesis, hypoxia, metabolism and the pathways regulating the response to external stimuli can now be targeted and monitored at a very early stage and at a molecular level.

In the field of optical tomographic imaging, increasingly used for pre-clinical research, a wide variety of probes have been developed enabling the specific targeting of many different molecular functions. In addition, the ability to use fluorescing proteins with animal cancer models makes monitoring the progress of disease straightforward. Optical tomographic techniques can provide 3D imaging of fluorescence light emitted from the probe or protein [5, 6]. In the case studied and presented here a Fluorescence Molecular Tomography (FMT) system is used to image signal emitted from HeLa cancer cells expressing the red emitting protein Katushka injected subcutaneously in the hind limb flank of mice. Imaging performed longitudinally provides a direct monitoring of the growing tumor [7].

II. Materials and Methods

A. Animal preparation

For the studies presented here Rag1-/- immunodeficient mice were used. Katushka expressing HeLa cancer cells were injected subcutaneously and grown as xenografts in the hind limb flanks. Initially $5x10^5$ cells were injected and tumors were allowed to grow until 4-10mm in diameter. Animals were kept anaesthetized using isoflurane throughout the preparation and imaging procedures. A small tumor (typically <1mm diameter) was generally visible within 4-5 days following the injection, at which point imaging was initiated, while the mice were sacrificed 11-20 days after implantation, depending on tumor size.

B. Experimental procedure

The experimental system used for *in-vivo* imaging comprises a series of laser sources employed according to the fluorescence target. A diode laser (Soliton-GmbH, Germany) emitting at 592nm was used to excite Katushka as close to the absorption maximum as possible. A cooled 16-bit CCD (Andor BV-434, Belfast, Northern Ireland) camera was used

for the detection of signals. Light collection was performed through a 50mm Macro f/2.8 objective (SIGMA Corporation, Tokyo, Japan) and different interference bandpass filters (Andover Corporation, USA) for isolating the fluorescence and excitation signals. In the case presented here, fluorescence was acquired using a 700/75nm filter, whereas no filter was used for the excitation. The system can be operated in both transmission and reflection geometry, however, in this study only reflection measurements were done since the targets were superficially located. An optical scanner was employed to scan the laser source into the desired points on the surface of the subject. In all experiments described here 49 illumination points were used in a 7x7 arrangement.

III. *IN-SILICO* MODELS AND TOMOGRAPHIC IMAGING

A. In-silico model

The mathematical model, presented here, is a deterministic, continuum model of reaction-diffusion type that describes the spatial ($\boldsymbol{x}$) and temporal (t) evolution of cancer cells and its microenvironment at population level [12, 13]. The tumor microenvironment consists of the vasculature that provides oxygen to cancer cells and tumor-induced angiogenic factors (e.g., VEGF). Depending on oxygen supply, cancer cells can be proliferative, hypoxic or necrotic. The system of the coupled reaction-diffusion equations of the concentrations of these species is shown in (1).

$$\frac{\partial c}{\partial t} = \nabla \cdot (D_c(1-T)\nabla c) + \rho c(1-T) + \gamma ho - \beta c(1-o) - a_n nc$$

$$\frac{\partial h}{\partial t} = \nabla \cdot (D_h(1-T)\nabla h) - \gamma ho + \beta c(1-o) - (a_h(1-o) + a_n n)h$$

$$\frac{\partial n}{\partial t} = a_h h(1-o) + a_n n(c+h+v) \quad (1)$$

$$\frac{\partial o}{\partial t} = \nabla \cdot (D_o \nabla o) + \beta_o v - \gamma_{oc} c - \gamma_{oh} h$$

$$\frac{\partial v}{\partial t} = \nabla \cdot (D_v(1-T)\nabla v) + \mu \frac{a}{K_m + a} v(1-T) - a_n nv$$

$$\frac{\partial a}{\partial t} = \nabla \cdot (D_a \nabla a) + \delta_c c + \delta_h h - q\mu \frac{\alpha}{K_m + \alpha} v(1-T) - \omega av - \lambda a$$

The first equation describes the evolution of normoxic cell density, $c(\boldsymbol{x}, t)$. Normoxic cells possess a random motility D_c, proliferate at a rate ρ, turn to hypoxic at a rate β (when oxygen is inadequate) and turn directly to necrotic cells (due to contact death) at a rate a_n. Similarly, the second equation describes the evolution of hypoxic cells, $h(\boldsymbol{x}, t)$. Hypoxic cells diffuse at a rate D_h, turn back to normoxic cells at a rate γ (if oxygen supply increases) and turn to necrotic at a rate a_h (if oxygen is insufficient). The rates β and γ are made proportional to metabolic rate ρ and reflect the cellular response time to changes in the environment. The third equation shows the evolution of necrotic cells, $n(\boldsymbol{x}, t)$. Continuing, oxygen (o) is produced by vasculature at a rate β_o, diffuses at a rate D_o and is consumed by normoxic and hypoxic cells at a rate γ_{oc} and γ_{oh}, respectively. Endothelial cells (forming the vasculature), $v(\boldsymbol{x}, t)$, diffuse randomly at a rate D_v, proliferate at a rate a_v, which depends on the concentration of angiogenic factors according to the Monod model ($a_v = \mu \frac{a}{K_m + a}$, μ is the maximal proliferation rate of endothelial cells and K_m is the Michaelis–Menten constant reflecting the response of endothelial cells to angiogenic factors) and turn to necrotic cells at a rate a_n. Lastly, angiogenic factors, $a(\boldsymbol{x}, t)$, diffuse in the tissue at a rate D_a, are produced by normoxic and hypoxic cells at a rate δ_c and δ_h, respectively, taken up by endothelial cells with a coefficient q, decay at a rate λ and are washed out by vessels at rate ω. In these equations, $T = (c + h + v + n)/k$, where k corresponds to the tumor cell carrying capacity. The term $(1 - T)$ is used to reflect the inhibition of motility and proliferation due to cellular crowding.

This model was initially used to simulate glioma growth [12], but was adapted in this work to meet the growth pattern of HeLa cells by significantly decreasing diffusion coefficients and proliferation rate, as found in [15]. The rest parameter values used in this model are in accordance to [12, 13]. The spatiotemporal solution of the system is approximated by applying numerical schemes of Finite Differences in two spatial dimensions. Implementation details can be found in [15].

C. Tomographic imaging

Tomographic imaging was performed by raster scanning the laser source into selected illumination points on the subject, taking care that the scanning area covers the targeted tumor. For each illumination point two measurements are recorded sequentially, by selecting the appropriate filters as described above: the excitation light diffusely reflected back to the camera and the fluorescence light emitted by the Katushka expressing cancer cells. The two measurements were then combined in the tomographic algorithm to produce the 3D reconstructions. Light propagation was modeled by Diffusion Theory, while a normalized calculation approach was used to combine the two acquired intensities [8, 9]. Reconstructions were performed with an iterative method with a mesh size of 26x26x6 voxels giving an axial resolution of 0.5mm and a depth resolution of 0.8mm [10, 11]. The result is a 3D reconstruction of the fluorescence intensity that can be associated to the cancer tumor and when longitudinal studies are performed, monitor its growth over time.

IV. RESULTS

In this section the results from *in-vivo* imaging and the *in-silico* model applied to the requirements of the specific mouse model are presented.

A. In-vivo tumor growth

As described above to monitor tumor growth *in-vivo* animals were imaged for several days and fluorescence data were analyzed for each imaging session in order to obtain the growth curve of the tumor. Characteristic images of the excitation and fluorescence signals recorded during the study can be seen in Fig. 1b and c. These excitation and fluorescence data were obtained by summing up the raw images for all illumination points. Data in Fig. 1 correspond

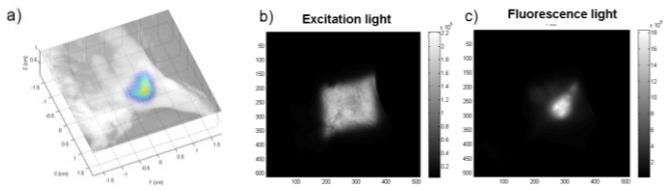

Figure 1. 2D raw data obtained during *in-vivo* imaging of tumor growth in a mouse model. a) 3D fluorescence reconstruction image showing the tumor in the flank of the mouse. b) image of the excitation light showing the scanning area and c) image of the fluorescence light emitted by the Katushka expressing HeLa cells.

to day 9 after the injection of the HeLa cells where a clear tumor can be observed with a size of *circa* 4-5mm.

Fig. 1a presents the fluorescence reconstruction in 3D overlaid on the white light image of the animal. The data from the reconstructions from each day were then used to obtain the growth curve of the specific tumor. This was performed by calculating the mean fluorescence intensity of the reconstruction and then plotting against time (days). Results are presented in Fig. 3a (red-square-pointed line) where reconstructed fluorescence intensity divided by the reconstructed fluorescence intensity at day 9 after injection (relative growth) is plotted as a function of time and compared with the *in-silico* predictions (blue line). A fast onset of growth is observed for the first 3 days, which is then slowed down until a plateau is reached after the 7th day. This behavior can be explained by the complexity of the tumor environment that cannot always maintain a constant balance of supply and demand of nutrients and can be simulated by the *in-silico* model, as presented in the following section.

B. In-silico tumor growth

In order to simulate tumor growth, we used the mathematical model described in section III. The system of equations (1) were solved in a 100×100 grid spanning an overall area of $L \times L$ for $L = 2cm$. The temporal resolution was set to $\tau = 8h$. In order to simplify the simulations and compensate for missing parameter values, the model was non-dimensionalized as described in [13]. Thus, $\hat{x} = \frac{x}{L}$, $\hat{t} = \frac{t}{\tau}, \hat{c} = \frac{c}{k}, \hat{h} = \frac{h}{k}$, $\hat{n} = \frac{n}{k}$, $\hat{v} = \frac{v}{k}$ and $\hat{a} = \frac{a}{a_{max}}$, where $k = 2.39\ 10^8 \frac{cells}{cm^3}$ and $a_{max} = 5.75\ 10^{-6} \frac{mmol}{cm^3}$.

The complete set of the parameter values used in the model are depicted in Table I. The proliferation rate of HeLa cells is set according to [14]. For simplicity, in all simulations described here, the initial distribution that describes the vasculature is assumed homogeneous. However, it must be stressed that similar results have been obtained (data not shown) when initialize vasculature with various heterogeneous distributions. The oxygen concentration is initialized at its saturation value ($o(\boldsymbol{x}, 0) = 1$) and the initial concentration of angiogenic factors is assumed zero ($a(\boldsymbol{x}, 0) = 0$). For simplicity, the tumor population is assumed to initially consist of only normoxic cells. Thus, $h(\boldsymbol{x}, 0) = 0$ and $n(\boldsymbol{x}, 0) = 0$, although hypoxia must have been developed in the real tumor at day 9 after injection. The initial distribution of normoxic cells ($c(\boldsymbol{x}, 0)$) is approximated with i) a Gaussian distribution of standard deviation $\sigma_x = \sigma_y = 0.13cm$ (model A) and ii) the fluorescence intensity distribution of a 2D-depth slice at day 9 (model B), as shown in Fig. 2a. Although the reconstructed fluorescence intensity is linear with viable fluorescing cells allowing for relative comparisons, the exact correspondence between fluorescence intensity values and cell population is missing. Therefore, the initial normoxic distributions are allowed to attain various maximum values. To compare the simulations with the in-vivo growth curve, the total sum of normoxic and hypoxic concentrations in the computational grid is calculated at each simulation time point and divided by the initial sum of normoxic and hypoxic concentrations (relative growth).

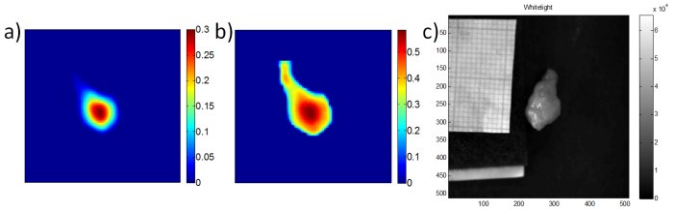

Figure 2. a) Initial distribution of normoxic cells in proportion to fluorescence intensity feeding model B, b) The predicted distribution of viable (normoxic plus hypoxic) cells after 8 fictitious days (day17) c) White light image showing the tumor the day the mouse was sacrificed (day 17). The tumor is approximately 7mm in diameter.

The simulations suggest that in order to achieve the observed growth curve and avoid saturation of cellular concentrations as indicated by fluorescence measurements, the initial tumor population must be sparsely distributed. For model B, the maximum value of the initial normoxic concentration is set to 0.3. We intentionally initialize model A with a Gaussian distribution of smaller standard deviation than the initial size of the tumor in order to additionally demonstrate its previous exponential growth phase. The initial height of the Gaussian model A is set to 0.05. It is important to mention that alternative sets of modeling parameters concerning specifically the level of tumor vascularization ($v(\boldsymbol{x}, 0)$), the maximum value of the initial

TABLE I – THE PARAMETERS FOR PIHNA MODEL SIMULATION AND THEIR NONDIMENSIONALIZED VERSIONS

Parameter	Value	Nondim.	Parameter	Value	Nondim.	Parameter	Value	Nondim.
T_c	$18.24\ \left(\frac{days}{cell}\right)$	T_c	δ_c	$7.59\ 10^{-16}\left(\frac{mmol}{cell\ day}\right)$	$\frac{\tau k}{a_{max}}\delta_c$	D_a	$2.9\ 10^{-7}\left(\frac{cm^2}{s}\right)$	$\frac{\tau}{L^2}D_a$
ρ	$\frac{ln2}{T_c}\left(\frac{1}{day}\right)$	$\tau\rho$	δ_h	$1.43\ 10^{-12}\left(\frac{mmol}{cell\ day}\right)$	$\frac{\tau k}{a_{max}}\delta_h$	K_m	$5.75\ 10^{-7}\left(\frac{mmol}{cm^3}\right)$	$\frac{K_m}{a_{max}}$
γ	$0.1\rho\left(\frac{1}{day}\right)$	$\tau\gamma$	β	$\rho\left(\frac{1}{day}\right)$	$\tau\beta$	λ	$\frac{ln2}{64}\left(\frac{1}{min}\right)$	$\tau\lambda$
a_n	$0\left(\frac{1}{day}\right)$	0	D, D_v, D_c, D_h	$10^{-11}\left(\frac{cm^2}{s}\right)$	$\frac{\tau}{L^2}D$	ω	$2.17\ 10^{-6}\left(\frac{1}{cell\ day}\right)$	$\tau k\omega$
a_h	$\frac{\rho}{100}\left(\frac{1}{day}\right)$	τa_h	β_o	-	100	μ	$\frac{ln2}{15}\left(\frac{1}{day}\right)$	$\tau\mu$
D_o	$10^{-5}\left(\frac{cm^2}{s}\right)$	$\frac{\tau}{L^2}D_o$	γ_{oc}	$6.25\ 10^{-17}\left(\frac{M}{cell\ sec}\right)$	70	γ_{oh}	–	30

normoxic distribution, and the normoxic-hypoxic conversion rates β and γ, which are all interrelated and determine the cellular composition within tumor, can lead to similar results.

Interestingly, as can be seen in Fig. 2b the shape predictions of the final tumor for model B are similar to the ex-vivo data (Fig. 2c). As can be seen in Fig. 3a, the predicted growth curves of both model A (blue line) and model B (green line) are inline with the in-vivo observations (red-square-pointed line) and well approximate the fast growth of the first days and the following slowdown phase of tumor cells. This behavior can be explained by the increasing hypoxia within tumor (Fig. 3b). Angiogenic factors triggered by hypoxic cells initiate endothelial proliferation and a new vasculature is established (data not shown). Yet, the new vasculature is insufficient for the increasing metabolic demands of cancer cells. As depicted in Fig. 3c, tumor size also reaches a plateau after several days of growth. In accordance to in-vivo experiments, model B estimates that the tumor diameter increases from 5 to 7mm within 8 days. Furthermore, the simulations show that low diffusion rate of cancer cells (model C) is important for the tumor growth to reach a plateau (Fig. 3a-black line).

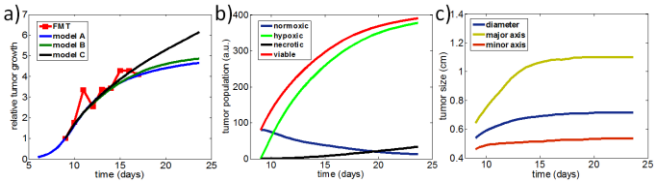

Figure 3. a) in-vivo obtained growth curve (red-square-pointed line) is compared with in-silico predictions. Model A (blue line) is initialized with a Gaussian distribution. The exponential phase prior to measurements (day 9) can be seen. Model B (green line) is initialized with the fluorescence intensity distribution of a 2D-depth slice assuming that the maximum value of the initial distribution is 0.3. Model C (black line) is similar to Model B but the diffusion coefficient of cancer cells is 10^3 times larger than in Model B. b) The temporal evolution of normoxic (blue line), hypoxic (green line), necrotic (black line) and viable cells (red line) for model B and c) the estimated tumor size as a function of time.

V. Discussion

Fig. 4 illustrates a high linear correlation between *in silico* prediction and *in vivo* captured data. Furthermore, the simulations suggest that nutrient competition is a key determinant for explaining the growth behavior of the tumor under study. The simulations show the importance of proper initialization in predicting the evolution of tumor and challenge for additional microscopic information to drive the in-silico model.

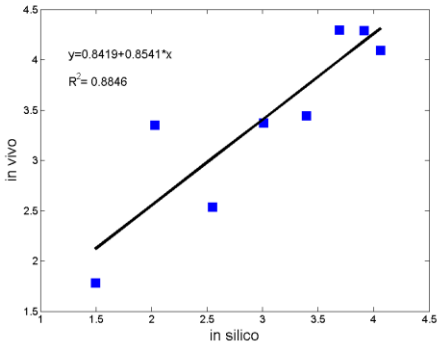

Figure 4. Plot showing the comparison between in vivo and in silico obtained values. A clear linear relation is observed.

VI. Conclusion

Current models proposed in the modeling community are either incomplete or inapplicable in the clinical practice mainly because the output provided is highly variable and parameter dependent. Hundreds of parameters are non-specified or intuitively used based on theoretical concepts. Molecular functional imaging techniques, especially Fluorescence Molecular Tomography, provide the means to assess parameters in-vivo and validate the outcome of the predictions. Further work in this direction is expected to demonstrate the potential for clinical translation of the proposed models by increasing confidence in the clinical community.

References

[1] L. B. Edelman, J. A. Eddy, and N. D. Price, "In silico models of cancer," Wiley Interdiscip Rev Syst Biol Med, vol. 2, pp. 438-59, Jul-Aug 2010.

[2] S. Sanga, H. B. Frieboes, X. Zheng, R. Gatenby, E. L. Bearer, and V. Cristini, "Predictive oncology: a review of multidisciplinary, multiscale in silico modeling linking phenotype, morphology and growth," Neuroimage, vol. 37 Suppl 1, pp. S120-34, 2007.

[3] R. Weissleder, M. J. Pittet, "Imaging in the era of molecular imaging", Nature, vol. 452, pp. 580-589, April 2008.

[4] T. F. Massoud, S. S. Gambhir, "Integrating noninvasive molecular imaging into molecular medicine: an evolving paradigm"*Trends Mol Med*vol. 13, pp.183-91 May 2007

[5] R. Weissleder, V. Ntziachristos, "Shedding light into live molecular targets", nat. Med., vol. 9, pp. 123-128, January 2003

[6] V. Ntziachristos, J. Ripoll, L. V. Wang, R. Weissleder, "Looking and listening to light: the evolution of whole-body photonic imaging",*Nat Biotechnol*vol. 23, pp. 313-20 March 2005.

[7] G. Zacharakis, H. Kambara, H. Shih, J. Ripoll, J. Grimm, Y. Saeki, R.Weissleder, V.Ntziachristos, "Volumetric tomography of fluorescent proteins through small animals in vivo",*ProcNatlAcadSci U S A*vol. 102, pp. 18252-18257, December 2005

[8] V. Ntziachristos, R. Weissleder, "Experimental three-dimensional fluorescence reconstruction of diffuse media by use of a normalized Born approximation", *Opt. Lett.* vol. 26, pp. 893-5 June 2001.

[9] G. Zacharakis, J. Ripoll, R. Weissleder, and V. Ntziachristos, "Fluorescent Protein Tomography scanner for small animal imaging," *IEEE Trans. Med. Imaging*, vol. 24, pp. 878 - 885, July 2005.

[10] C. Kak and M. Slaney, *Principles of Computerized Tomographic Imaging*, New York:IEEE, 1988, ch. 7.

[11] J. Ripoll, R. B. Schultz, V. Ntziachristos, "Free-Space Propagation of Diffuse Light: Theory and Experiments", Phys. Rev. Lett. vol. 91, pp. 103901-1-103901-4, September 2003

[12] K. R. Swanson, R. C. Rockne, J. Claridge, M. A. Chaplain, E. C. Alvord Jr, and A. Anderson, "Quantifying the role of angiogenesis in malignant progression of gliomas: In Silico modeling integrates imaging and histology," *Cancer Res*, vol. 71, pp. 7366-7375, 2011

[13] P. Hinow, P. Gerlee, *et al.,* "A spatial model of tumor-host interaction: application of chemotherapy," Math BiosciEng,vol. 6, no. 3, pp. 521-46, 2009

[14] P. Jaluria**,** M. Betenbaugh**,** K. Konstantopoulos and J. Shiloach, "Enhancement of cell proliferation in various mammalian cell lines by gene insertion of a cyclin-dependent kinase homolog," BMC Biotechnology, vol. **7**, no.71, 2007

[15] A. Roniotis, V. Sakkalis, E. Tzamali, et al., "Solving the PIHNA model while accounting for radiotherapy," *5th Int. Adv. Research Workshop on In Silico Oncology and Cancer Investigation (IARWISOCI 2012)*, Oct 22-23, Athens, Greece, 2012.